

ACCEPTED VERSION

R. Tamblyn, T. Zack, A.K. Schmitt, M. Hand, D. Kelsey, L. Morrissey, S. Pabst, I.P. Savov
Blueschist from the Mariana forearc records long-lived residence of material in the subduction channel

Earth and Planetary Science Letters, 2019; 519:171-181

©2019 Elsevier B.V. All rights reserved.

This manuscript version is made available under the CC-BY-NC-ND 4.0 license
<http://creativecommons.org/licenses/by-nc-nd/4.0/>

Final publication at <http://dx.doi.org/10.1016/j.epsl.2019.05.013>

PERMISSIONS

<https://www.elsevier.com/about/policies/sharing>

Accepted Manuscript

Authors can share their [accepted manuscript](#):

24 Month Embargo

After the embargo period

- via non-commercial hosting platforms such as their institutional repository
- via commercial sites with which Elsevier has an agreement

In all cases [accepted manuscripts](#) should:

- link to the formal publication via its DOI
- bear a CC-BY-NC-ND license – this is easy to do
- if aggregated with other manuscripts, for example in a repository or other site, be shared in alignment with our [hosting policy](#)
- not be added to or enhanced in any way to appear more like, or to substitute for, the published journal article

2 September 2021

<http://hdl.handle.net/2440/120882>

1 Blueschist from the Mariana forearc
2 records long-lived residence of material in the
3 subduction channel

4 Tamblyn, R.¹, Zack, T.^{1,2}, Schmitt, A. K.³, Hand, M.¹,
5 Kelsey, D.^{1*}, Morrissey, L.⁴, Pabst, S.⁵, Savov, I.P.⁶

6 ¹ Department of Earth Sciences, University of Adelaide, Adelaide, Australia

7 ² Department of Earth Sciences, University of Gothenburg, Gothenburg, Sweden

8 ³ Institut für Geowissenschaften, Universität Heidelberg, Germany

9 ⁴ School of Natural and Built Environments, University of South Australia, Adelaide, Australia

10 ⁵ BHP Billiton Iron Ore, Exploration, PO Box 655, Newman, WA 6753, Australia

11 ⁶ School of Earth and Environment, University of Leeds, Institute of Geophysics and Tectonics, UK

12 *Current Address: Geological Survey of Western Australia, East Perth, Western Australia, Australia

13 Corresponding author: Renée Tamblyn (renee.tamblyn@adelaide.edu.au)

14
15 **Highlights**

- 16 • Blueschist from serpentine mud volcano in Mariana forearc is ca. 50 Ma old
- 17 • The mineral assemblage records warm metamorphic conditions during IBM subduction
18 initiation
- 19 • Blueschist rocks have resided in the subduction channel for at least 46 Ma

20

21

22

23

24

25
26
27
28
29
30
31
32
33
34
35
36
37
38
39
40
41
42
43
44
45
46
47
48
49
50
51
52

Abstract

From ca. 50 Ma to present, the western Pacific plate has been subducting under the Philippine Sea plate, forming the oceanic Izu-Bonin-Mariana (IBM) subduction system. It is the only known location where subduction zone products are presently being transported to the surface by serpentinite-mud volcanoes. A large serpentine mud “volcano” forms the South Chamorro Seamount and was successfully drilled by ODP during Leg 195. This returned mostly partially serpentinitized harzburgites enclosed in serpentinite muds. In addition, limited numbers of small (1 mm–1 cm) fragments of rare blueschists were also discovered. U–Pb dating of zircon and rutile from one of these blueschist clasts give ages of 51.1 ± 1.2 Ma and 47.5 ± 2.0 Ma, respectively. These are interpreted to date prograde high-pressure metamorphism. Mineral equilibria modelling of the blueschist clast suggests the mineral assemblage formed at conditions of ~ 1.6 GPa and ~ 590 °C. We interpret that this high-pressure assemblage formed at a depth of ~ 50 km within the subduction channel and was subsequently exhumed and entrained into the South Chamorro serpentinite volcano system at depths of ~ 27 km. Consequently, we propose that the material erupted from the South Chamorro Seamount may be sampling far greater depths within the Mariana subduction system than previously thought. The apparent thermal gradient implied by the pressure–temperature modelling (~ 370 °C/GPa) is slightly warmer than that predicted by typical subduction channel numerical models and other blueschists worldwide. The age of the blueschist suggests it formed during the arc initiation stages of the proto-Izu-Bonin-Mariana arc, with the P – T conditions recording thermally elevated conditions during initial stages of western Pacific plate subduction. This indicates the blueschist had prolonged residence time in the stable forearc as the system underwent east-directed rollback. The Mariana blueschist shows that subduction products can remain entrained in subduction channels for many millions of years prior to exhumation.

53
54
55
56
57
58
59
60
61
62
63
64
65
66
67
68
69
70
71
72
73
74
75
76
77
78
79
80

1. Introduction

From ca. 50 Ma until present, the Western Pacific plate has been subducting under the Philippine Sea plate, forming the oceanic Izu-Bonin-Mariana (IBM) arc-basin system (Figure 1; Stern and Bloomer, 1992; Ishizuka et al., 2011, 2018). This system provides an opportunity to study active processes within convergent intra-oceanic settings such as magmatism, seismicity, element recycling and hydrothermal transport. It is also the only known location on Earth where subduction zone products are actively transported to the surface by serpentinite-mud volcanoes (e.g. Fryer, 2012; Pabst et al., 2012). These serpentinite-mud volcanoes occur up to 90 km away from the trench axis in the forearc region (Figure 1; Fryer et al., 2006). In the southern Mariana segment, these volcanoes are interpreted to currently sample slab-generated fluids from a depth of up to 27 km (Fryer, 2012), offering a unique window into processes operating at shallow depths during subduction and in the mantle wedge above.

Previous studies on the variety of hard rock clasts “erupted” from these serpentinite-mud volcanoes have used them to infer the chemical and physical conditions of the subducting slab surface at shallow depths under the Mariana forearc (Savov et al., 2005; Fryer et al., 2006; Pabst et al., 2012). A major assumption from all previous studies is that the clasts and muds are derived from recently subducted products and hence are representative of the modern subduction system, however this assumption has never been tested. Additionally, there has been no in-depth and detailed metamorphic work done on the clasts to constrain the metamorphic conditions of formation and therefore the depth they sample within the subduction system. A high-pressure

81 origin for blueschist clasts from the Mariana serpentinite-mud volcanoes has been suggested
82 before, but never quantified (Maekawa et al., 1993; Fryer et al., 2006; Yamamoto et al., 1995).
83 Because these metamorphic clasts contain a wealth of information about the thermal conditions
84 within the slab, as well as potentially providing avenues to determine the age of metamorphic
85 recrystallization, they can provide unique insights into the residence times of material within
86 subduction channels formed by ocean-ocean plate convergence.

87

88 This study is focused on one mafic clast (195-1200E-1H-3-4b), recovered from serpentinite mud
89 drilled during ODP Leg 195 at Site 1200 at the summit of the active South Chamorro Seamount
90 (Figure 1; see Pabst et al. (2012) for further description on this sample). Clasts recovered from the
91 drilling were predominately serpentinite fragments, however rare blueschist-facies metamafic
92 fragments were also recovered. While multiple clasts contained blueschist-facies mineral
93 assemblages (including amphibole, chlorite, epidote and phengite), one rare sample contained
94 rutile and zircon which could be targeted for geochronology. We derive constraints on the
95 thermobarometric conditions recorded by this sample, and the age of metamorphism. The results
96 provide insight into the depth of material return to the surface, and the subduction channel P - T
97 conditions during the very beginning of Mariana subduction.

98

99 **2. Background**

100 *2.1 Geology and geometry of the IBM system*

101

102 The IBM system is generated by the westward directed subduction of the Pacific oceanic plate
103 under the Philippine Sea, which initiated at ca. 51 Ma (Figure 1; Reagan et al., 2010; Ishizuka et
104 al., 2018). The northern IBM trench segment (Izu-Bonin) shows an increasing dip of the Wadati-
105 Benioff zone from $\sim 40^\circ$ in the north to $\sim 80^\circ$ in the south, with intermediate-depth seismicity
106 occurring between depths of ~ 150 to ~ 300 km (Gvirtzman and Stern, 2004). In contrast, the
107 southern IBM segment (Mariana) has a subvertical Wadati-Benioff zone, with deep (>300 km)

108 seismic events (Gvartzman and Stern, 2004). As such, the width of the subduction zone interface
109 between the overriding and subducting plates increases along the IBM from north to south
110 (Gvartzman and Stern, 2004). While this only delineates the current subduction zone structure
111 under the IBM, it is useful for interpretations of subduction channel dynamics which presently
112 operate. Currently, the slab in the Mariana segment is in a state of rollback, as the Pacific and
113 Philippine plates are both advancing westwards, with the latter at a slightly faster rate (Gvartzman
114 and Stern, 2004). Complex geometries involving slab tearing and steepening in the southern
115 segment of the IBM have led to the extreme dip and hence depth of the trench in this area
116 (Gvartzman and Stern, 2004). The Mariana forearc is extensively faulted, due to oblique
117 convergence as well as the curvature produced by back-arc extension, resulting in it being
118 dominated by sinistral shear (Stern et al., 2003). This structural architecture is probably a crucial
119 factor in allowing serpentinitized mantle to exhume and rise to the surface, driving serpentinite-mud
120 volcanism. The Mariana forearc is the only place on modern Earth where this occurs (Fryer et al.,
121 1992, 1999, 2000, 2006; Fryer, 2012;).

122

123 The recent history of the IBM is well studied. However, the cause for subduction inception in the
124 IBM is the source of much debate, due to lack of access to the earliest subduction-generated rocks
125 (e.g. Arculus et al., 2015; 2016). However, the Jurassic oceanic crust to the east formed a west-
126 dipping subduction zone under the Philippine Sea or Pacific crust. The timing of this is estimated
127 to be ca. 51–47 Ma (Ishizuka et al, 2011, 2018). Ar–Ar whole rock ages for initial construction of
128 the Mariana arc match those for the Izu-Bonin arc at ca. 49–47 Ma, while forearc basement from
129 the IBM has been dated by Ar–Ar to have formed by at least ca. 47–45 Ma (Cosca et al., 1998).
130 More recently, the basement of the IBM arc was dated by Ar–Ar geochronology at 48.7 ± 0.3 Ma
131 (Ishizuka et al., 2018). This age is further supported by nano and microfossils in the overlying
132 volcanoclastic sediments (Arculus et al., 2015). A ca. 51 Ma age is reported based on stratigraphic
133 relationships for tholeiitic fore-arc basalts interpreted to be the first lavas to erupt when the Pacific
134 plate initially sunk under the Philippine plate (Reagan et al., 2010; 2017). This has been further

135 supported by a U–Pb zircon age of 51.1 ± 1.5 from gabbro underlying the fore-arc basalts
136 (Ishizuka et al., 2011). Regardless of the exact timing of initiation, it seems that subduction
137 initiation along the 2800 km IBM system occurred over 51–47 Ma (Stern et al., 2003; Arculus et
138 al., 2015). The Kyushu-Palau Ridge (Figure 1) was active from ca. 48 Ma to ca. 25 Ma, and is the
139 result of a stable magmatic arc during which the IBM subduction system was essentially immobile
140 (Ishizuka et al., 2011). Spreading in the mid-southern Parece Vela Basin began after this (Figure
141 1a), and further spreading in the northern Izu-Bonin segment commenced at ca. 25 Ma with both
142 terminating around 15 Ma due to collision of the northern IBM with Honshu (Stern et al., 2003).
143 In the southern segment, eastwards rollback resulted in extension to form the Mariana Trough (~6
144 Ma back-arc basin), with the onset of seafloor spreading at ca. 3–4 Ma (Yamazaki and Stern,
145 1997). As such, the inception of the currently active Mariana Arc (Figure 1a; the West Mariana
146 Ridge) is interpreted to be 3–4 Ma old (Stern et al., 2003), and the remnant arc was left behind.
147 Over this Eocene–Pleistocene evolution, the relative slab rollback to the east has resulted in two
148 former oceanic arcs younging from the Palau-Kyushu Ridge (active from the onset of subduction
149 to ca. 25 Ma), to the current Mariana Ridge (Figure 1a).

150

151 *2.2 Previous studies of blueschists from the Mariana forearc drill sites*

152

153 A series of active mud volcanoes occur on the upper plate between the arc (the Mariana Ridge)
154 and the Mariana Trough (current trench; Figure 1a). The two most intensely studied active
155 seamounts are the South Chamorro Seamount and the Conical Seamount, which occur 85 and 90
156 km from the trench respectively (Fryer et al., 1999; Savov et al., 2005). Deep sea drilling of these
157 serpentinite seamounts (ODP Legs 125 and 195) returned predominantly serpentinitized harzburgite
158 and dunite clasts, but also rare metabasic blueschist clasts (~5% of clasts) in a matrix of fine
159 serpentinite muds (Savov et al., 2004; Fryer and Salisbury, 2006; Fryer et al., 2006). These clasts
160 have been divided into amphibole-talc-chlorite-schists, chlorite-epidote-schists, amphibole-
161 chlorite-phengite-schists and mono-mineralic aggregates of talc or amphibole (Pabst et al., 2012).

162

163 A variety of metamafic clasts as well as matrix serpentinite muds have been studied to make
164 inferences about the pressure–temperature (P – T) conditions within and below the Conical and
165 South Chamorro seamounts. Blueschist clasts were discovered during drilling of the Conical
166 Seamount in the northern Mariana forearc (east of Asuncion; Figure 1b) by Maekawa et al. (1993),
167 who reported the first direct evidence for low temperature and relatively high-pressure
168 metamorphism in a subduction zone. These blueschists were estimated to have formed at
169 temperatures of 150–250 °C and pressures of 5–6 kbar (potentially corresponding to depths of 16–
170 20 km), based on the presence of aragonite, the compositions of sodic pyroxenes and temperature
171 dependence of inferred metamorphic reactions (Maekawa et al., 1993). Maekawa et al. (1995) also
172 noted the existence of lawsonite-bearing blueschist clasts, and indicated that higher grade
173 metamorphic rocks may be sourced from below the seamount. Numerous blueschist clasts were
174 recovered from Conical Seamount drilled during ODP Leg 125. These were analysed for their
175 whole rock geochemistry by Yamamoto et al. (1995), who concluded the volcano was returning
176 clasts derived from a MORB source.

177

178 Blueschist clasts drilled from the summit of the South Chamorro Seamount to the east of Guam
179 were recovered only recently (Figure 1b; Shipboard Scientific Party, 2000). Due to similar jadeitic
180 (Jd) compositions of their pyroxenes, Pabst et al. (2012) estimated that blueschists from the South
181 Chamorro Seamount had reached similar P – T conditions as those from Conical Seamount, studied
182 by Maekawa et al. (1993; 1995). Further comparisons of the metamorphic mineral assemblages of
183 the blueschists from South Chamorro Seamount with those of the Franciscan Complex have been
184 used to infer conditions of 250–300 °C and 7 kbar for the late-stage blueschist facies assemblage
185 (Pabst et al., 2012). Fryer et al. (2006) estimated conditions of ~250–300 °C and 4–5 kbar based
186 on assumed equilibrium of epidote with magnesioriebeckite/barroisite from a different metabasite
187 schist from South Chamorro Seamount. Higher grade conditions for metamorphic products have
188 also been suggested by Murata et al. (2009) from the existence of antigorite in serpentized
189 peridotites. Antigorite coexisting with clinopyroxene and olivine indicates high-temperature
190 serpentization between ~450–550 °C, leading Murata et al., (2009) to suggest possible tectonic

191 cycling of mantle wedge material. Additionally, temperatures and pressures of 350 °C and 8 kbar
192 have been estimated for the source of serpentinite muds of the South Chamorro Seamount (Fryer et
193 al., 2000), corresponding to depths of ~25–27 km. Fryer (1992) and Fryer et al. (2006) suggested
194 that blueschists record higher grade conditions than those of the slab interface directly below the
195 seamount, however no quantitative P – T estimates have been made. Geochemical and seismic
196 studies, as well as earthquake locations on the subducting Pacific plate, have been used to suggest
197 the mud volcanoes are sampling the slab interface at depth of 27–29 km (Oakley et al., 2008;
198 Savov et al., 2005; Fryer et al., 2000). This is also generally supported by temperatures of ~200–
199 300 °C estimated from chrysolite, lizardite and brucite-bearing serpentinitized peridotites
200 (D’Antonio and Kristensen, 2004). Fryer et al. (2006) suggested that MORB and OIB samples
201 must have been derived from subducted oceanic plate buried to a depth of up to 30 km. This would
202 suggest that the variety of clasts erupted from the South Chamorro Seamount and by inference
203 other serpentinite volcanos in the Marianas forearc are being sampled from the slab interface
204 beneath the volcano. While some of the geochemical signature of the fluid released from the South
205 Chamorro Seamount appears to be originating from the currently subducting Pacific slab surface at
206 a depth of ~27 km (Mottl et al., 2004), studies on the metamorphic conditions of the blueschist
207 fragments span a range of P – T conditions.

208

209 In addition to the only limited constraints on the P – T conditions recorded by the metamorphic
210 clasts, there is also lack of age data. While not overtly stated, existing studies on the mud hosted
211 clasts assume they record modern conditions on the slab interface. However studies (Krebs et al.,
212 2008; Lázaro et al., 2009; Blanco-Quintero et al., 2011) from high-pressure rocks in ancient
213 serpentinite mélanges show that they may contain a range of metamorphic ages, indicating that
214 material can reside within subduction zone channels for potentially tens of millions of years.

215

216 3. Methods

217

218 The ~ 2×2 mm blueschist clast recovered from ODP Site 1200 was mounted in epoxy resin and
219 polished. It was primarily mapped in BSE using a Quanta 600 SEM at Adelaide Microscopy,
220 University of Adelaide, using Mineral Liberation Analysis software, to determine petrological
221 relationships and mineral modal proportions in the clast.

222

223 Quantitative Electron probe microanalysis (EPMA) elemental mapping used a CAMECA SXFive
224 equipped with 5 wavelength-dispersive spectrometers (WDS) and X-Ray detectors, running the
225 PeakSite software. Beam conditions were set at an accelerating voltage of 15 kV and 100 nA,
226 utilising a focussed beam. Compositional mapping was done at a 4 µm pixel resolution. Pixel
227 dwell time in all maps was set to 40 ms. Calibration and quantitative data reduction of maps was
228 carried out with the “Probe for EPMA” software, distributed by Probe Software Inc. Calibration
229 was performed on certified natural and synthetic standards from Astimex Ltd and P&H Associates.
230 The clast was mapped for 10 elements using their K α lines, thus requiring two mapping passes on
231 the five spectrometers (Pass 1: Ca, Na, P, Mg, Fe; Pass 2: Ti, Si, Al, Mn, K). Potentially mobile
232 elements were analysed in the first pass. The average minimum detection limits (at the 99%
233 confidence interval) in wt.% for the quantitative maps were: Ca (0.06), Na (0.12), Ti (0.07), Mg
234 (0.08), Fe (0.17), K (0.06), Si (0.01), P (0.08), Al (0.08), Mn (0.16).

235

236 The X-ray maps were then used to identify the metamorphic mineral assemblages and mineral
237 modal proportions were determined by pixel counting using image analysis software. Although the
238 blueschist clast contains some coarse-grained minerals, is generally medium-grained. As such,
239 these modal proportions are reasonably representative of the local equilibrium volume. The modal
240 proportion and electron microprobe compositions of mineral assemblages was used to compute a
241 bulk chemical composition for petrological modelling (Supplementary Data Table 1). We chose
242 this approach to determine a bulk composition as the sample was considered too valuable to be
243 consumed for conventional-style geochemical analysis. Ti-magnetite was omitted from the bulk
244 rock chemistry calculations, based on textural evidence it is magmatic. Allanite and zircon were
245 also omitted as they contain elements that cannot be modelled. Results of pixel counting and

246 associated calculations to construct the bulk composition are shown in Supplementary Data Table
247 2.
248
249 Mineral equilibria forward modelling was undertaken using THERMOCALC v 3.4 in the
250 NCFMASHTO system, using the internally consistent thermodynamic dataset 'ds55' (filename tc-
251 ds55.txt; November 2003 updated version of the Holland and Powell 1998 dataset) and activity-
252 composition models in Diener et al. (2012) and references within. The calculated K and Mn
253 concentrations in the calculated bulk rock composition are near zero, therefore K and Mn were
254 excluded from the model system. Pumpellyite was not predicted in the modelling, possibly due to
255 lack of a pumpellyite activity-composition model that allows solid solution. Calculations to test
256 the sensitivity of modelled mineral equilibria to H₂O content using P-M_{H₂O} models demonstrated
257 the mineral assemblage, modal proportions and compositions recorded by the sample are stable
258 over a large range of H₂O contents (from 9 mol% to more than 13 mol %, Supplementary Figure
259 1). As a specific value could not be pinpointed, and the sample evidently formed under water-rich
260 conditions as indicated by abundant chlorite, amphibole and epidote, modelling was done with
261 water in excess, i.e. defining H₂O as a saturating phase. Oxidation state (Fe₂O₃, or O in the bulk
262 rock chemistry) was constrained from a P-M_O model (Supplementary Figure 2), where mineral
263 modal proportions and compositions overlapped in the interpreted peak field at approximately
264 M(O) = 0.55, or O = 1.97 mol%. This value directly overlaps with recalculated mineral
265 microprobe chemical analyses used to calculate the bulk rock chemistry by assuming perfect
266 mineral stoichiometry in the calculation of cations from the wt% oxide data (Droop, 1987; Leake
267 et al., 1997). Contouring of the mineral equilibria models was calculated using the software
268 TCInvestigator (Pearce et al., 2015). This produces contoured diagrams of normalised abundances
269 (modes) of minerals, as well as mineral compositional contours, which can then be matched with
270 measured EPMA data and calculated mineral modes of the sample to further constrain the
271 pressure-temperature conditions experienced.

272

273 Secondary ionization mass spectrometry (SIMS) U-Pb geochronology was carried out using a
274 CAMECA ims 1270 ion microprobe at the University of California of Los Angeles
275 (Supplementary Data Table 3). In-situ analyses targeted zircon in the polished blueschist block
276 using methods for analysis of small grains in their matrix as described in Schmitt et al. (2010).
277 Rutile analyses were also performed in situ on the same mount, but due to the larger grain size of
278 rutile compared to zircon, nearly full transmission was reached in the ion microprobe's field
279 aperture. Instrumental set-up for rutile analysis is summarized in Schmitt and Zack (2012); all ages
280 are reported relative to AS3 reference zircon (1099 Ma; Paces and Miller, 1993) and R10b
281 reference rutile (1090 Ma; Luvizotto et al., 2009).

282

283 4. Results

284

285 4.1 Petrography

286 The blueschist clast (E1H3-4b) is dominated by an amphibole and chlorite-bearing matrix, with
287 less abundant epidote, rutile, titanite and allanite, and very rare pumpellyite, phengite and
288 clinopyroxene (Figure 2). Amphibole is typically ~10–200 μm in size and zoned (Figure 3; 4),
289 with patchy magnesio-hornblende cores, surrounded by volumetrically dominant edenite/pargasite,
290 and then a sharply-defined thin rim of magnesiokatophorite (Figure 5a, nomenclature follows
291 Leake et al., 1997). This zonation can be seen in element maps (Figure 4a), with a marked increase
292 in Na and Fe from core to rim, a decrease in Mg and Ca from core to rim, and high SiO_2 cores and
293 rims and corresponding low alumina cores and rims. Small needle-like grains of actinolite also
294 occur within the amphibole. Chlorite is commonly usually less than 50 μm , but rare grains are up
295 to 300 μm in size. It is weakly zoned with thin rims that are comparatively poor in Fe and Al but
296 rich in Si and Mg (Figure 3b, Figure 5b). It forms irregular grains intergrown with amphibole and
297 epidote as well as narrow veins which cross-cut or occur along amphibole cleavage planes.
298 Epidote occurs as smaller (occasionally up to ~250 μm) grains within amphibole or chlorite. It
299 regularly overgrows texturally early allanite (Figure 2), and is unzoned, except for a thin rim of

300 elevated Fe (Figure 5c, increase of ~1.65 wt% Fe₂O₃; Supplementary Data Table 1). Allanite is up
301 to 80 μm in size and oscillatory zoned in rare earth elements (Figure 2), consistent with
302 metamorphic allanite grown in the presence of fluid. Ti-magnetite (~10–100 μm) is overgrown by
303 rims of rutile (up to ~100 μm across). Titanite forms discontinuous overgrowths on the rutile and
304 Ti-magnetite which are up to 40 μm wide (Figure 2), and also occurs as euhedral crystals with
305 amphibole and chlorite. Minor (<1%) fine-grained (5–20 μm) pumpellyite is associated with
306 retrograde titanite and chlorite. Rare fine-grained clinopyroxene (<10 μm) occurs in the chlorite-
307 amphibole matrix, and contains 7–26 mol% jadeite (Figure 5d, Pabst et al., 2012). Very fine-
308 grained rare phengite occurs as needles in amphibole, and fine-grained zircon up to 10 μm also
309 occurs in amphibole and epidote. The main mineral assemblages are: 1) early Na-rich amphibole
310 core, chlorite, epidote, clinopyroxene and rutile, and 2) late Na-Fe rich amphibole rims, actinolite,
311 titanite, and pumpellyite. Quartz is absent, and is typically absent from most blueschists from
312 South Chamorro (Pabst et al., 2012).

313

314 *4.2 Zircon and rutile geochronology*

315 Textually resolved in-situ SIMS U–Pb geochronology (Figure 6) yields concordia ages of $47.5 \pm$
316 2.0 Ma (mean square of weighted deviates MSWD of concordance = 0.00052; $n = 9$) for rutile, and
317 51.1 ± 1.2 Ma (MSWD = 0.16; $n = 4$) for zircon (Figure 7; Supplementary Data Table 3). U
318 abundances in rutile range between 11 and 30 ppm, and corresponding radiogenic ²⁰⁶Pb yields are
319 between 42 and 95%. U abundances in zircon range from ~180 to ~1300 ppm, with high
320 radiogenic ²⁰⁶Pb yields of >97% in favourable cases. Zirconium in rutile has on average 380 ppm,
321 which corresponds in the presence of zircon and absence of quartz to a maximum temperature of
322 650 °C using the Tomkins et al. (2007) calibration at pressures 1.5 GPa derived from mineral
323 equilibria modelling (see below).

324

325 *4.3 Mineral equilibria modelling*

326

327 A peak to retrograde P – T evolution can be inferred from the compositional isopleths of amphibole
328 as well as the modal proportions of metamorphic minerals for the modelled mineral equilibria.
329 Compositions of amphibole cores are taken from EPMA analyses of magnesio-hornblende,
330 magnesio-hastingsite and pargasite, and amphibole rim compositions from analyses of magnesio-
331 katophorite (Figure 5; Supplementary Data Table 1; Pabst et al, 2012). Modal proportions of
332 minerals are converted from volume % as measured by pixel counting, to one-oxide-normalized
333 %, compliant with the modes computed by THERMOCALC (Supplementary Data Table 2; Figure
334 8). Uncertainties on the calculations in the mineral equilibria model are 2 sigma and are shown in
335 Supplementary Figure 3. The peak assemblage consists of chlorite + amphibole + epidote +
336 clinopyroxene (diopside) + rutile, and is bound by the disappearance of clinopyroxene and the
337 addition of hematite to higher temperatures, and the solid-solution transition of diopside to
338 omphacite (across the clinopyroxene solvus) at lower temperatures and higher pressures. The peak
339 assemblage occurs over a large range of conditions, from 1.1 ± 0.07 GPa and 515 ± 9 °C to $1.8 \pm$
340 0.06 GPa and 600 ± 21 °C (Figure 8a). The retrograde evolution is characterized by the formation
341 of titanite and calcic amphibole, evidenced by the presence of titanite coronas on rutile and small,
342 late actinolite needles within amphibole. Clinopyroxene is interpreted to be relict from the peak
343 assemblage, and therefore the retrograde path also involves the loss of clinopyroxene. The P – T
344 path can be further constrained using amphibole compositional isopleths. Compositional
345 parameters A (xNa on the A site), C (xCa on the M4 site) and Z (xNa on the M4 sites) were
346 calculated from amphibole microprobe data and plotted on the mineral equilibria model (grey
347 fields with dashed lines). Compositional isopleths of the amphibole cores plot over a wide range of
348 pressures and temperatures, from 1.2–1.7 GPa and 540–600 °C, with average errors on each
349 compositional range of ± 0.07 GPa and 12 °C (Figure 8b). Corresponding model proportions of the
350 amphibole cores from 1.5–1.7 (± 0.06) GPa and 575–600 (± 12) °C (Figure 8b). Although not
351 definitive, it is likely the compositions and modal proportions of the magnesio-hornblende cores
352 point to a high-pressure history that predated the formation of the texturally dominant assemblage
353 in the rock. Modal proportion isopleths of chlorite, total amphibole and epidote within the

354 modelled peak field span from 1.1–1.45 GPa and 540–590 °C with average errors of 0.07 GPa and
355 10 °C, and also occur in retrograde P – T space with the addition of titanite (Figure 8b). The
356 compositions of amphibole rims (magnesiokatophorite) plot within the field of the retrograde
357 mineral assemblage from 0.7–0.9 GPa and 470–495 °C, with average errors of 0.06 GPa and 9 °C
358 (Figure 8b).

359

360 *4.4 Protolith constraints*

361 The investigated sample has an unusual whole rock composition, with 44.2 mol% SiO₂ and 22 mol%
362 MgO (Supplementary Data Table 2). Technically it can be labelled a picrite, which is not typically
363 observed in likely protoliths such as MORB, OIB or former arc basement. A more realistic scenario
364 to explain the bulk rock composition is the formation of a hybrid rock composition derived from
365 MORB with a metasomatic imprint from surrounding hydrated mantle, similar to that observed on
366 Catalina Island (e.g. Bebout and Barton 2002; Pabst et al., 2012). The implication is that the
367 investigated sample was not part of a coherent subducting slab at the time of zircon and rutile
368 formation. Another likely protolith could be an already metasomatized and/or metamorphosed
369 fragment, as have been reported from the Mariana forearc (Fryer et al., 2006; Pabst et al., 2012).

370

371

372 **5. Discussion**

373

374 Texturally, rutile in blueschist clast E1H3-4b forms part of a typical high-pressure metamorphic
375 assemblage (Zack & Kooijman, 2017). Furthermore rutile is extremely rare as an igneous mineral
376 in mafic rocks, and the chance that the erupted clast sampled a metamorphosed mafic rock with
377 relic igneous rutile would appear negligible. Zircon is relatively common in mafic subvolcanic
378 and plutonic rocks as a late-crystallizing igneous mineral, however in general it is not abundant in
379 MORB. A magmatic zircon age from crystallisation of the subducting slab for the zircon can
380 probably be dismissed as the age of oceanic crust being subducted into the IBM system is Jurassic
381 (Stern et al., 2003). Moreover, the similarity in age to the rutile also strongly implies a

382 metamorphic origin. Hence, the U–Pb ages from rutile and zircon are interpreted to record the
383 high-pressure metamorphism.

384
385 Texturally, rutile rims early magmatic Ti-magnetite (Figure 6a). Regardless of the P – T path taken
386 by the clast, rutile growth would have occurred on the prograde path (Figure 8), and continued to
387 be stable to the peak conditions. To demonstrate this, black dashed lines on the mineral equilibria
388 model indicate the stabilization of rutile (rutile in) and the maximum rutile mode reached (Figure
389 8a), after this mode line rutile abundance is unchanging as it does not continue to grow. As the
390 closure temperature of U–Pb diffusion in rutile is estimated to be ca. 600–640 °C (Zack &
391 Kooijman 2017), the age of ca. 47.5 Ma most likely represents the growth of rutile during prograde
392 metamorphism.

393
394 The mechanism of metamorphic zircon formation in low-temperature metamorphic rocks is still
395 not well understood. Zircon occurs in the clast as small (5–50 μm) euhedral grains within matrix
396 amphibole and epidote/allanite (Figure 6b,c). Metamorphic zircon in blueschist-facies mafic rocks
397 is thought to grow as a result of either dissolution-precipitation of inherited zircon, or release of
398 zirconium through the breakdown of higher temperature minerals such as magmatic pyroxene (e.g.
399 Rubatto and Hermann, 2007) and granulite-facies rutile (Zack & Kooijman 2017). There is no
400 evidence for relic inherited zircon or textural features suggesting dissolution-precipitation (Rubatto
401 and Hermann, 2007; Rubatto et al., 2008). Possible mechanisms of zircon growth in the sample are
402 the breakdown of Zr-bearing magmatic minerals which persisted to high pressures (Rubatto and
403 Hermann, 2007). Breakdown of Ti-magnetite to form zircon (+ rutile + Fe-phase) on the prograde
404 path would result in both minerals producing similar ages as they were formed in the same
405 reaction. Alternatively, breakdown of magmatic clinopyroxene to amphibole also may release
406 zirconium, and may have been the source during prograde metamorphism (Rubatto et al., 2008).
407 While the exact prograde reaction that formed zircon is unclear, the closure temperature of U–Pb
408 diffusion in zircon is estimated to be >900 °C (Cherniak and Watson, 2001). Therefore, the Eocene

409 age is interpreted to record growth of zircon during metamorphism that occurred very soon after
410 subduction initiation.

411

412 The mineral equilibria modelling results indicate a peak to retrograde evolution from ~ 1.6 GPa to
413 0.8 GPa. Although the exact P – T points are poorly constrained, the path is strongly supported by
414 textural relationships within the sample, measured mineral modal proportions, and the
415 compositions of zoned amphibole. It is possible to suggest a higher-pressure peak assemblage at
416 approximately 1.6 ± 0.2 GPa and 585 ± 20 °C, followed by a retrograde evolution towards $\sim 0.8 \pm$
417 0.15 GPa and 485 ± 30 °C. These conditions range in approximate apparent thermal gradients from
418 ~ 370 °C/GPa at peak, and ~ 600 °C/GPa during the retrograde evolution, with an average of
419 around 470 °C/GPa. These approximations could be within error of uncertainties within the
420 mineral equilibria model (Supplementary Figure 1), and the geochronology from the clast only
421 constrains the prograde part of this evolution. However, if it is not within error of the mineral
422 equilibria model uncertainties, the change in thermal gradient may reflect changes in subducting
423 slab geometry, as the slab becomes steeper at greater depth, resulting in lower thermal gradients at
424 depth (Peacock, 2003; Syracuse et al., 2010; Penniston-Dorland et al., 2015). Alternatively, the
425 change in thermal gradient could be due to the advection of heat within the rising serpentinite
426 melange that carried the blueschist clast to comparatively shallow depths within the subduction
427 channel (Gerya et al., 2002). These pressure-temperature conditions are in line with measured
428 global subduction zone data (Figure 9a,b,c; Penniston-Dorland et al., 2015; Brown and Johnson,
429 2017; Agard et al., 2018). When compared to numerical models (Figure 9d; Gerya et al., 2002;
430 Syracuse et al., 2010; van Keken et al., 2011; Ruh et al., 2018), the pressure-conditions are slightly
431 above average, all though this may be due to the exclusion of shear heating as a model parameter
432 (e.g. Kohn et al., 2018). Combined with the U–Pb rutile and zircon geochronology, the P – T data
433 suggests the blueschist clast records initially warm conditions relative to numerical models during
434 the early initiation of subduction of the Pacific plate (ca. 52 Ma; Ishizuka et al., 2011; 2018; Agard
435 et al., 2018). During the early stages of subduction, conditions are generally warmer, as the plate

436 subducts at a shallower angle, and the ‘dragging down’ of geotherms at the base of the overlying
437 mantle wedge has not yet been significantly achieved (Gerya et al., 2002). This is in line with
438 ‘warm’ pressure-temperature estimates from newly initiated subduction zones that have also been
439 recorded by high-pressure mafic rocks (Figure 9c; Agard et al., 2018).

440

441 Forearc and reararc basalts mark the initiation of subduction in the Mariana system, and are
442 immediately followed by forearc boninite magmatism from 48.2–45.1 Ma (Reagan et al., 2008;
443 Ishizuka et al., 2011; Arculus et al., 2015; Reagan et al., 2017). The eruption of these boninites
444 necessitates the interaction of very depleted mantle wedge with slab-derived fluids at shallow
445 depths during subduction, and was coeval with blueschist metamorphism (this study). The
446 similarity between the metamorphic ages obtained in this study and the age of boninitic
447 magmatism, as well as the higher than usual thermal gradients recorded by the mineral
448 assemblage, supports the existence of a hot mantle wedge above a warm subduction channel
449 during early stages of subduction initiation in the Marianas.

450

451 If only lithostatic pressure is assumed, then the pressure estimates correspond to depths ranging
452 from ~46 km to ~25 km. Therefore, it appears the retrograde P – T path essentially ends at
453 conditions corresponding to the slab depth below the South Chamorro Seamount (~27 km; Pabst et
454 al., 2012; Fryer et al., 2006). ODP Site 1200 is on the summit of the seamount (Figure 1b;
455 Shipboard Scientific Party, 2000), and therefore it can be assumed that the drill core represents
456 most recent mud extrusions from the serpentinite-mud volcano (Fryer et al., 2006). The oldest
457 magmatic volcanism in the current Mariana arc (or Mariana ridge, Figure 1b) is interpreted to be
458 ca. 3–4 Ma (Stern et al., 2003), and as such the position of the subduction zone and the maximum
459 age of the serpentinite volcanoes is reasonably inferred as being similar. However, the rutile and
460 zircon ages record metamorphism at ca. 50 Ma. This suggests that the clast was trapped
461 somewhere within the subduction channel for at least ca. 46 Ma. The preservation of mineral
462 assemblages that record ‘warm’ peak metamorphic conditions, as well as metamorphic rutile and
463 zircon with Eocene ages, can be explained by either residence at peak depths for a significant

464 portion of the metamorphic history of the clast, or that this clast was exhumed to shallower depths
465 under the forearc and resided at cool conditions where recrystallization of minerals to lower
466 pressure-temperature assemblages was not achieved. Unfortunately, there are no geochronologic
467 constraints on when the blueschist was exhumed from depth to distinguish between these
468 possibilities. The lack of retrograde recrystallisation may suggest that the small clast was protected
469 from fluids and may have been armoured within a larger blueschist boudin or ‘knocker’, as
470 commonly occur in high-pressure metamorphic and serpentinite mélanges such as the Franciscan
471 Complex and Carribean (cf. Becker and Cloos, 1985; Lázaro et al., 2009; Blanco-Quintero et al.,
472 2011). While the lack of geochronology on the retrograde history of the rock precludes definite
473 explanation, it seems likely that the clast was exhumed to a shallow refrigerated region under the
474 forearc in the Mariana subduction channel some time between ca 49 and 3 Ma, prior to its eruption
475 in the mud volcano (Figure 10). However, the exact mechanism of this exhumation from ca. 50 km
476 deep remains unknown. It could have occurred as return flow of the hydrated serpentinite mantle
477 wedge cycled high-pressure material as the Mariana subduction system matured and steepened
478 (Gerya et al., 2002). Alternatively, detachment and slicing of oceanic crust within the subduction
479 channel could have allowed partial exhumation of the blueschist-facies material (Ruh et al., 2015;
480 Agard et al., 2018). Regardless, given that the clast is erupted in a serpentinite-mud volcano,
481 serpentinite-driven buoyancy appears to have been an important part of the exhumation
482 mechanism.

483
484 Implicit in the above scenario is that the blueschist must have formed during the early stages of
485 subduction under the proto-IBM arc. A number of workers (e.g. Cosca et al., 1988; Reagan et al.,
486 2008; 2010; Ishizuka et al., 2018), have argued that subduction initiated at around 51–47 Ma ago.
487 High-pressure metamorphism at ca. 50 Ma supports the upper scale of those scenarios. The current
488 location of the trench is ~ 1300 km to the east of the ridge (Figure 1a), as slab rollback has resulted
489 in extension of the Philippine Sea Plate. This means that the forearc not only entrapped and
490 preserved the blueschist clast, but it also survived at least partly intact in its ~1300 km long
491 eastward journey transported by slab rollback. A similar scenario has been suggested for long-

492 lived (>40 Ma) entrapment of high-pressure metamorphic rocks in serpentinite mélangé in other
493 oceanic subduction systems such as the Caribbean and the Franciscan Complex (Krebs et al.,
494 2008; Lázaro et al., 2009; Blanco-Quintero et al., 2011).

495

496 The age and source region of the blueschist clast sampled from the South Chamorro seamount has
497 implications for interpretations and future models regarding subduction zone conditions inferred
498 from past studies on erupted clasts and muds from these seamounts. Some authors (Fryer et al.,
499 1992; Savov et al., 2005; Fryer et al., 2006; Murato et al., 2009), have indicated that subduction
500 products from serpentinite volcanoes may be sampled from greater depths than the slab
501 immediately below the mud volcano and therefore have more complex source regions. However,
502 they have been unable to quantify those depths. These authors have also assumed that the material
503 exhumed in the mud volcanism was recently subducted. As such, the data has been used to
504 describe ongoing Mariana trench subduction systematics, when in fact the subduction zone retains
505 an integration of material from its inception until recently. The inferred depth from the modelled
506 metamorphic assemblage in the blueschist clast indicates that the ‘plumbing system’ of the
507 Marianas mud volcanoes is much more temporally and spatially complex than previously thought,
508 meaning the metamorphic clasts in the IBM mud volcanoes capture a long history of the chemical
509 and thermal evolution of the western Pacific slab. This temporally and spatially complex range of
510 sources for material from the mud volcanoes means that caution should be exercised when
511 interpreting data from clasts or muds erupted from seamounts in the Mariana forearc.

512

513 **6. Conclusions**

514

515 Detailed petrographic analyses and mineral equilibria forward modelling of a blueschist clast from
516 the South Chamorro Seamount in the Mariana forearc indicates the mud volcano samples material
517 from depths of ca. 50 km, which is well below the current depth of the slab directly below the
518 volcano. The modelled P – T conditions (ca. 1.6 GPa and 590 °C) of the blueschist clast indicate the
519 thermal regime was warmer than typical oceanic subduction, suggesting the modelled mineral

520 assemblage formed in the initial stages of the IBM subduction system. This is consistent with
521 concordant U–Pb ages of ca. 50 Ma from rutile and zircon within the blueschist assemblage,
522 confirming the mineral assemblage formed soon after the Pacific plate began subducting under the
523 Philippine Sea plate. Maturation of the subduction zone and formation of serpentinite within the
524 subduction channel then facilitated return flow, driving exhumation of the blueschist clast to a
525 refrigerated region under the forearc for at least ca. 46 Ma, before it was erupted in the South
526 Chamorro mud volcano in the Mariana forearc. During this period of time there was ~1300 km of
527 east-directed slab rollback, which transported the blueschist and other early subduction products
528 with it. Therefore the South Chamorro Seamount, and by inference other volcanoes in the Mariana
529 forearc, are probably sampling a temporally and spatially diverse range of lithologies and P – T – t
530 histories that document the thermal evolution of the surface of the subducting plate over time. The
531 data from the Mariana system suggests that potential serpentinite hosted blueschist and eclogite
532 blocks in ancient subduction product complexes (e.g. Franciscan and Caribbean) may hold
533 extensive records of the thermal evolution of subducting slabs.

534

535 **Acknowledgements**

536 We would like to thank Ben Wade of Adelaide Microscopy for his assistance running element
537 maps. We also thank E. Baxter and P. Agard for their thoughtful reviews, and M. Bickle for his
538 editorial handling. This work was supported by ARC grant DP160104637 and DFG grant Za285/4.
539 The ion microprobe facility at UCLA is partly supported by a grant from the Instrumentation and
540 Facilities Program, Division of Earth Sciences, National Science Foundation.

541

542 **References**

543

544 Agard, P., Plunder, A., Angiboust, S., Bonnet, G., & Ruh, J. (2018). The subduction plate
545 interface: Rock record and mechanical coupling (from long to short time scales).
546 *Lithos*.

547 Arculus, R. J., Ishizuka, O., Bogus, K. A., Gurnis, M., Hickey-Vargas, R., Aljahdali, M. H., .
548 . . Drab, L. (2015). A record of spontaneous subduction initiation in the Izu-Bonin-
549 Mariana arc. *Nature Geoscience*, 8(9), 728-733.

550 Arculus, R. J., Ishizuka, O., Bogus, K. A., Gurnis, M., Hickey-Vargas, R., Aljahdali, M. H., .
551 . . Drab, L. (2016). Reply to 'Unclear causes for subduction'. *Nature Geoscience*, 9(5),
552 338.

553 Bebout, G. E., & Barton, M. D. (1993). Metasomatism during subduction: products and
554 possible paths in the Catalina Schist, California. *Chemical Geology*, 108(1-4), 61-92.

555 Becker, D. G., & Cloos, M. (1985). Mélange diapirs into the Cambria Slab: A Franciscan
556 trench slope basin near Cambria, California. *The Journal of Geology*, 93(2), 101-110.

557 Blanco-Quintero, I. F., García-Casco, A., & Gerya, T. V. (2011). Tectonic blocks in
558 serpentinite mélange (eastern Cuba) reveal large-scale convective flow of the
559 subduction channel. *Geology*, 39(1), 79-82.

560 Brown, M., & Johnson, T. (2018). Secular change in metamorphism and the onset of global
561 plate tectonics. *American Mineralogist*, 103(2), 181-196.

562 Cherniak, D., & Watson, E. (2001). Pb diffusion in zircon. *Chemical Geology*, 172(1), 5-24.

563 Cosca, M., Arculus, R. J., Perace, J., & Mitchell, J. G. (1998). $^{40}\text{Ar}/^{39}\text{Ar}$ and K–Ar
564 geochronological age constraints for the inception and early evolution of the Izu–
565 Bonin–Mariana arc system. *Island Arc*, 7(3), 579-595.

566 D'antonio, M., & Kristensen, M. (2004). Serpentine and brucite of ultramafic clasts from the
567 South Chamorro Seamount (Ocean Drilling Program Leg 195, Site 1200): inferences
568 for the serpentinization of the Mariana forearc mantle.

569 Diener, J., & Powell, R. (2012). Revised activity–composition models for clinopyroxene and
570 amphibole. *Journal of metamorphic Geology*, 30(2), 131-142.

571 Droop, G. (1987). A general equation for estimating Fe³⁺ concentrations in ferromagnesian
572 silicates and oxides from microprobe analyses, using stoichiometric criteria.
573 *Mineralogical Magazine*, 51(361), 431-435.

574 Fryer, P. (2012). Serpentinite mud volcanism: observations, processes, and implications.
575 *Annual review of marine science*, 4, 345-373.

576 Fryer, P., Gharib, J., Ross, K., Savov, I., & Mottl, M. (2006). Variability in serpentinite
577 mudflow mechanisms and sources: ODP drilling results on Mariana forearc
578 seamounts. *Geochemistry, Geophysics, Geosystems*, 7(8).

579 Fryer, P., Lockwood, J. P., Becker, N., Phipps, S., & Todd, C. S. (2000). Significance of
580 serpentine mud volcanism in convergent margins. *SPECIAL PAPERS-GEOLOGICAL*
581 *SOCIETY OF AMERICA*, 35-52.

582 Fryer, P., Pearce, J., & Stokking, L. (1992). 36. *A synthesis of Leg 125 drilling of serpentine*
583 *seamounts on the Mariana and Izu–Bonin forearcs*. Paper presented at the
584 Proceedings of the Ocean Drilling Program, Scientific Results.

585 Fryer, P., & Salisbury, M. (2006). *Leg 195 synthesis: Site 1200-Serpentinite seamounts of the*
586 *Izu-Bonin/Mariana convergent plate margin (ODP Leg 125 and 195 drilling results)*.
587 Paper presented at the Proc. ODP, Sci. Results.

588 Fryer, P., Wheat, C., & Mottl, M. (1999). Mariana blueschist mud volcanism: Implications
589 for conditions within the subduction zone. *Geology*, 27(2), 103-106.

590 Gerya, T. V., Stöckhert, B., & Perchuk, A. L. (2002). Exhumation of high-pressure
591 metamorphic rocks in a subduction channel: A numerical simulation. *Tectonics*,
592 21(6).

593 Gvirtzman, Z., & Stern, R. J. (2004). Bathymetry of Mariana trench-arc system and
594 formation of the Challenger Deep as a consequence of weak plate coupling.
595 *Tectonics*, 23(2).

596 Holland, T., & Powell, R. (1998). An internally consistent thermodynamic data set for phases
597 of petrological interest. *Journal of metamorphic Geology*, 16(3), 309-343.

598 Ishizuka, O., Hickey-Vargas, R., Arculus, R. J., Yagodzilski, G. M., Savov, I. P., Kusano,
599 Y., . . . Sudo, M. (2018). Age of Izu–Bonin–Mariana arc basement. *Earth and*
600 *Planetary Science Letters*, 481(Supplement C), 80-90. doi:
601 <https://doi.org/10.1016/j.epsl.2017.10.023>

602 Ishizuka, O., Tani, K., Reagan, M. K., Kanayama, K., Umino, S., Harigane, Y., . . . Dunkley,
603 D. J. (2011). The timescales of subduction initiation and subsequent evolution of an
604 oceanic island arc. *Earth and Planetary Science Letters*, 306(3), 229-240.

605 Krebs, M., Maresch, W., Schertl, H.-P., Münker, C., Baumann, A., Draper, G., . . . Trapp, E.
606 (2008). The dynamics of intra-oceanic subduction zones: a direct comparison between
607 fossil petrological evidence (Rio San Juan Complex, Dominican Republic) and
608 numerical simulation. *Lithos*, 103(1), 106-137.

609 Lázaro, C., García-Casco, A., Rojas Agramonte, Y., Kröner, A., Neubauer, F., &
610 ITURRALDE-VINENT, M. (2009). Fifty-five-million-year history of oceanic
611 subduction and exhumation at the northern edge of the Caribbean plate (Sierra del
612 Convento mélange, Cuba). *Journal of metamorphic Geology*, 27(1), 19-40.

613 Leake, B. E., Woolley, A. R., Arps, C. E., Birch, W. D., Gilbert, M. C., Grice, J. D., . . .
614 Krivovichev, V. G. (1997). Report. Nomenclature of amphiboles: report of the
615 subcommittee on amphiboles of the international mineralogical association
616 commission on new minerals and mineral names. *Mineralogical Magazine*, 61(2),
617 295-321.

618 Luvizotto, G., Zack, T., Meyer, H., Ludwig, T., Triebold, S., Kronz, A., . . . Klemme, S.
619 (2009). Rutile crystals as potential trace element and isotope mineral standards for
620 microanalysis. *Chemical Geology*, 261(3-4), 346-369.

621 Maekawa, H., Fryer, P., & Ozaki, A. (1995). Incipient Blueschist-Facies Metamorphism in
622 the Active Subduction Zone Beneath the Mariana Forearc. *Active margins and*
623 *marginal Basins of the Western pacific*, 281-289.

624 Maekawa, H., Shozul, M., Ishll, T., Fryer, P., & Pearce, J. A. (1993). Blueschist
625 metamorphism in an active subduction zone. *Nature*, 364(6437), 520-523.

626 Mottl, M. J., Wheat, C. G., Fryer, P., Gharib, J., & Martin, J. B. (2004). Chemistry of springs
627 across the Mariana forearc shows progressive devolatilization of the subducting plate.
628 *Geochimica et Cosmochimica Acta*, 68(23), 4915-4933.

629 Murata, K., Maekawa, H., Yokose, H., Yamamoto, K., Fujioka, K., Ishii, T., . . . Wada, Y.
630 (2009). Significance of serpentinization of wedge mantle peridotites beneath Mariana
631 forearc, western Pacific. *Geosphere*, 5(2), 90-104.

632 Oakley, A., Taylor, B., & Moore, G. (2008). Pacific Plate subduction beneath the central
633 Mariana and Izu-Bonin fore arcs: New insights from an old margin. *Geochemistry,*
634 *Geophysics, Geosystems*, 9(6).

635 Pabst, S., Zack, T., Savov, I. P., Ludwig, T., Rost, D., Tonarini, S., & Vicenzi, E. P. (2012).
636 The fate of subducted oceanic slabs in the shallow mantle: insights from boron
637 isotopes and light element composition of metasomatized blueschists from the
638 Mariana forearc. *Lithos*, 132, 162-179.

639 Paces, J. B., & Miller, J. D. (1993). Precise U-Pb ages of Duluth complex and related mafic
640 intrusions, northeastern Minnesota: Geochronological insights to physical,
641 petrogenetic, paleomagnetic, and tectonomagmatic processes associated with the 1.1

642 Ga midcontinent rift system. *Journal of Geophysical Research: Solid Earth*, 98(B8),
643 13997-14013.

644 Peacock, S. M. (2003). Thermal structure and metamorphic evolution of subducting slabs.
645 *Inside the subduction factory*, 7-22.

646 Pearce, M., White, A., & Gazley, M. (2015). TCInvestigator: automated calculation of
647 mineral mode and composition contours for thermocalc pseudosections. *Journal of*
648 *metamorphic Geology*, 33(4), 413-425.

649 Penniston-Dorland, S. C., Kohn, M. J., & Manning, C. E. (2015). The global range of
650 subduction zone thermal structures from exhumed blueschists and eclogites: Rocks
651 are hotter than models. *Earth and Planetary Science Letters*, 428, 243-254.

652 Reagan, M. K., Hanan, B. B., Heizler, M. T., Hartman, B. S., & Hickey-Vargas, R. (2008).
653 Petrogenesis of volcanic rocks from Saipan and Rota, Mariana Islands, and
654 implications for the evolution of nascent island arcs. *Journal of Petrology*, 49(3), 441-
655 464.

656 Reagan, M. K., Ishizuka, O., Stern, R. J., Kelley, K. A., Ohara, Y., Blichert-Toft, J., . . .
657 Hanan, B. B. (2010). Fore-arc basalts and subduction initiation in the Izu-Bonin-
658 Mariana system. *Geochemistry, Geophysics, Geosystems*, 11(3).

659 Reagan, M. K., Pearce, J. A., Petronotis, K., Almeev, R. R., Avery, A. J., Carvalho, C., . . .
660 Godard, M. (2017). Subduction initiation and ophiolite crust: new insights from IODP
661 drilling. *International Geology Review*, 59(11), 1439-1450.

662 Rubatto, D., & Hermann, J. r. (2007). Zircon behaviour in deeply subducted rocks. *Elements*,
663 3(1), 31-35.

664 Rubatto, D., Müntener, O., Barnhoorn, A., & Gregory, C. (2008). Dissolution-reprecipitation
665 of zircon at low-temperature, high-pressure conditions (Lanzo Massif, Italy).
666 *American Mineralogist*, 93(10), 1519-1529.

667 Ruh, J. B., Le Pourhiet, L., Agard, P., Burov, E., & Gerya, T. (2015). Tectonic slicing of
668 subducting oceanic crust along plate interfaces: Numerical modeling. *Geochemistry,*
669 *Geophysics, Geosystems, 16*(10), 3505-3531.

670 Savov, I., Tonarini, S., Ryan, J., & Mottl, M. (2004). *Boron isotope geochemistry of*
671 *serpentinites and porefluids from Leg 195, Site 1200, S. Chamorro Seamount,*
672 *Mariana forearc region.* Paper presented at the International Geological Congress
673 (IGC), Florence, Italy.

674 Savov, I. P., Ryan, J. G., D'Antonio, M., Kelley, K., & Mattie, P. (2005). Geochemistry of
675 serpentinitized peridotites from the Mariana Forearc Conical Seamount, ODP Leg 125:
676 Implications for the elemental recycling at subduction zones. *Geochemistry,*
677 *Geophysics, Geosystems, 6*(4).

678 Schmitt, A. K., Stockli, D. F., Lindsay, J. M., Robertson, R., Lovera, O. M., & Kislitsyn, R.
679 (2010). Episodic growth and homogenization of plutonic roots in arc volcanoes from
680 combined U–Th and (U–Th)/He zircon dating. *Earth and Planetary Science Letters,*
681 *295*(1-2), 91-103.

682 Schmitt, A. K., & Zack, T. (2012). High-sensitivity U–Pb rutile dating by secondary ion mass
683 spectrometry (SIMS) with an O₂⁺ primary beam. *Chemical Geology, 332,* 65-73.

684 Stern, R. J., & Bloomer, S. H. (1992). Subduction zone infancy: examples from the Eocene
685 Izu-Bonin-Mariana and Jurassic California arcs. *Geological Society of America*
686 *Bulletin, 104*(12), 1621-1636.

687 Stern, R. J., Fouch, M. J., & Klemperer, S. L. (2003). An overview of the Izu-Bonin-Mariana
688 subduction factory. *Inside the subduction factory,* 175-222.

689 Syracuse, E. M., van Keken, P. E., & Abers, G. A. (2010). The global range of subduction
690 zone thermal models. *Physics of the Earth and Planetary Interiors, 183*(1-2), 73-90.

691 Tomkins, H., Powell, R., & Ellis, D. (2007). The pressure dependence of the zirconium-in-
692 rutile thermometer. *Journal of metamorphic Geology*, 25(6), 703-713.

693 van Keken, P. E., Hacker, B. R., Syracuse, E. M., & Abers, G. A. (2011). Subduction factory:
694 4. Depth-dependent flux of H₂O from subducting slabs worldwide. *Journal of*
695 *Geophysical Research: Solid Earth*, 116(B1).

696 Yamamoto, K., Asahara, Y., Maekawa, H., & Sugitani, K. (1995). Origin of blueschist-facies
697 clasts in the Mariana forearc, Western Pacific. *Geochemical Journal*, 29(4), 259-275.

698 Yamazaki, T., & Stern, R. J. (1997). Topography and magnetic vector anomalies in the
699 Mariana Trough. *JAMSTEC J. Deep Sea Res*, 13, 31-45.

700 Zack, T., & Kooijman, E. (2017). Petrology and geochronology of rutile. *Reviews in*
701 *mineralogy and geochemistry*, 83(1), 443-467.

702

703

704

705

706 *Figure captions*

707

708 **Figure 1.** a) Bathymetric map of the Mariana segment of the IBM system, showing the tectonic
709 plates and ridges. Cross section is marked a' to b'. Location of South Chamorro Seamount is
710 indicated in black arrow. Modified from Fryer et al. (2002). b) 3D bathymetric image of South
711 Chamorro Seamount, indicated ODP drill site location after Savov et al (2005). c) Interpreted
712 cross section (a'–b') of the Mariana trench and forearc. Vertical exaggeration is 2:1. Plate
713 location and structure of the Philippine and Pacific plates after Fryer et al. (1999), Oakley et al.
714 (2008) and Pabst et al. (2012). Schematic representation of serpentinisation after Ruh et al.
715 (2015).

716

717 **Figure 2:** Mineralogical map of blueschist chip sample E1H3-4b, based on BSE imaging and
718 X-ray derived elemental maps. C and R correspond to examples of amphibole cores and rims.
719 Fine-grained minerals such as pumpellyite, clinopyroxene and zircon are not visible at this
720 scale.

721
722 **Figure 3:** Electron microprobe X-ray element maps of blueschist chip E1H3-4b. Black and
723 cooler colours indicate lower concentrations, whereas warmer colours indicates higher
724 concentrations. The maps are not quantitative and the colours scales from different maps do not
725 indicate the same numerical concentrations.

726
727 **Figure 4:** a) BSE and X-ray elemental maps of an amphibole grain from the blueschist clast.
728 Dotted white lines indicate the boundary of the core, main grain volume and sharp rim. b) BSE
729 and X-ray elemental maps of a chlorite grain that includes epidote (white core). Dotted line
730 indicates thin outer rim. The maps are not quantitative and the colours scales from different
731 maps do not indicate the same numerical concentrations.

732
733 **Figure 5:** Mineral composition plots. a) Amphibole compositions. b) Chlorite compositions. c)
734 Epidote compositions. d) Clinopyroxene compositions.

735
736 **Figure 6:** BSE images of locations of rutile and zircon targeted for U–Pb dating by Zack et al.
737 (2013). a) Metamorphic rutile rimming Ti-magnetite, further rimmed by retrograde titanite. b)
738 Zircon in the amphibole matrix. c) Zircon associated with metamorphic allanite/epidote. Ti-
739 mag: Ti-magnetite, Ru: Rutile, Ttn: Titanite, Ep: Epidote, Chl: Chlorite, Amph: Amphibole,
740 Zrc: Zircon, All: Allanite.

741

742 **Figure 7:** U–Pb Concordia for a) rutile and b) zircon analyses conducted on blueschist clast
743 sample E1H3-4b. Individual error ellipses (open) and error-weighted averages (filled) are
744 plotted at 95% confidence. Ages are calculated as concordia ages with probabilities of
745 concordance of 0.98 (rutile) and 0.69 (zircon) using Isoplot v.4.15 (Ludwig, 2012).

746

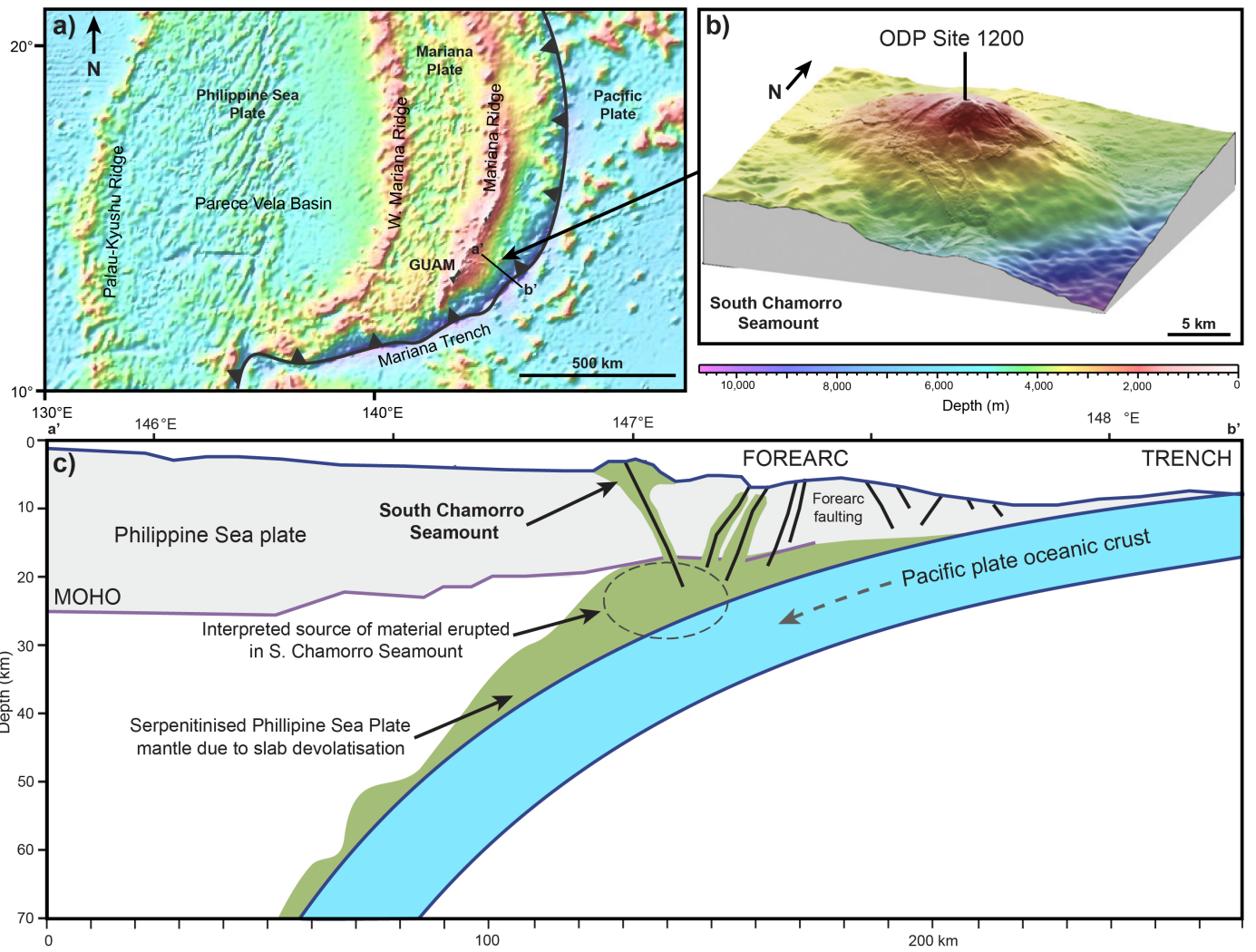
747 **Figure 8:** P – T mineral equilibria model for the blueschist chip, bulk composition used is in
748 upper left corner in mol %. a) Mineral equilibria model with inferred P – T path as a grey arrow,
749 dashed line represents unconstrained evolution. Fine black dotted line indicates rutile in and
750 maximum rutile modes. Variance is coloured where $v = 6$ is the darkest shade and variance
751 decreases as the shade lightens. Purple dashed lines indicate the locations of the omphacite-
752 diopside and actinolite-hornblende solvi. b) Mineral equilibria model with EPMA measured
753 ranges of amphibole compositions A (xNa on the A site), C (xCa on the M4 site) and Z (xNa on
754 the M4 sites, where the minimum and maximum values for each measured composition are
755 shown in grey dashed lines. Measured mineral modes (Supplementary Data Table 2) from the
756 sample are shown as solid coloured lines. Chl: chlorite, Amph: Amphibole, O: Omphacite, Di:
757 Diopside, Ep: Epidote, Ru: Rutile, Ttn: Titanite, Act: Actinolite, Gl: Glaucophane, Q: Quartz,
758 Ilm: Ilmenite, Hem: Hematite, Law: Lawsonite, G: Garnet.

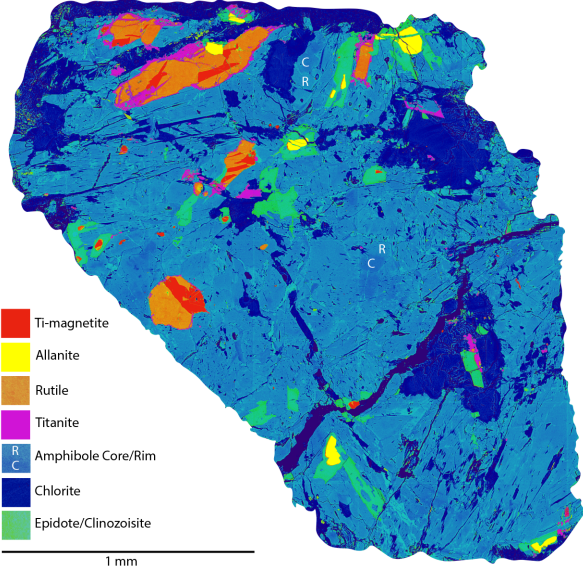
759

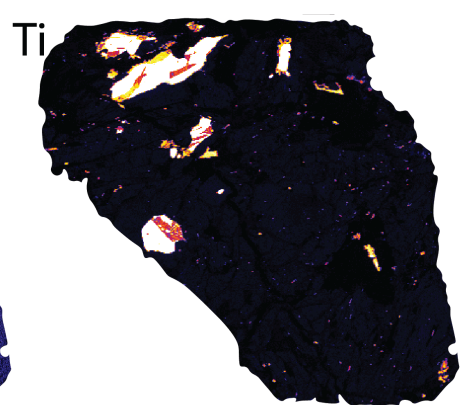
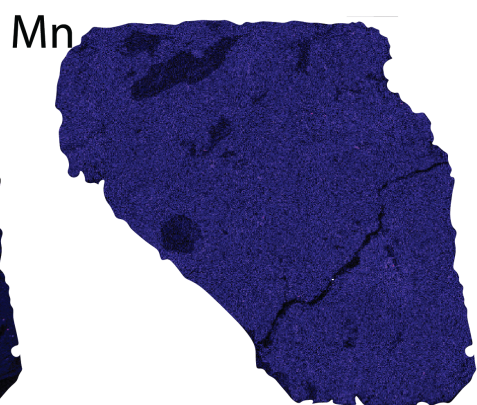
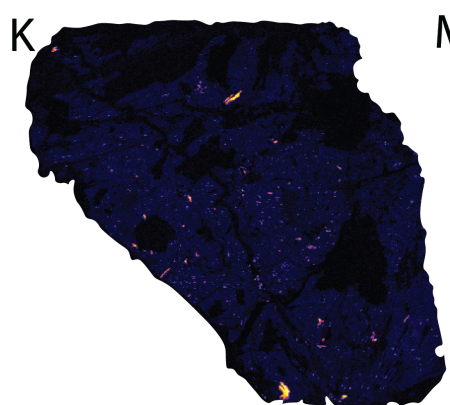
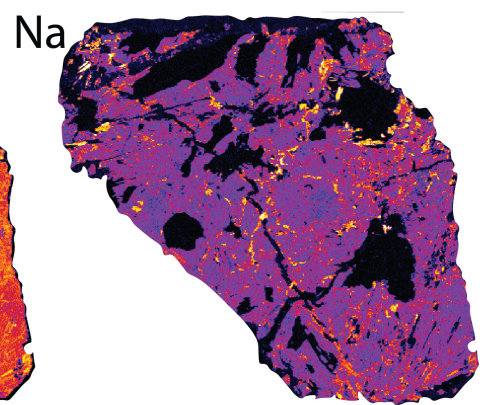
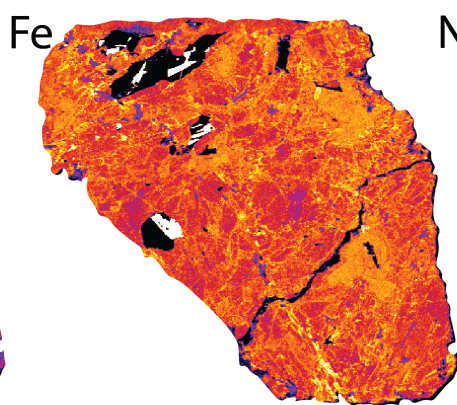
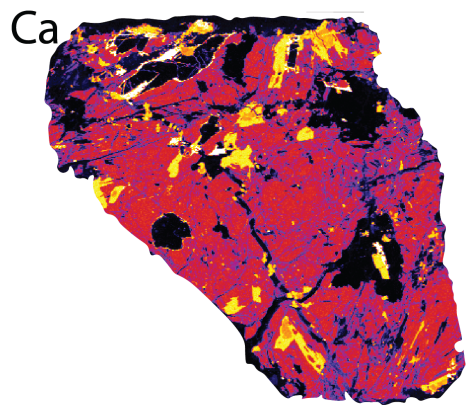
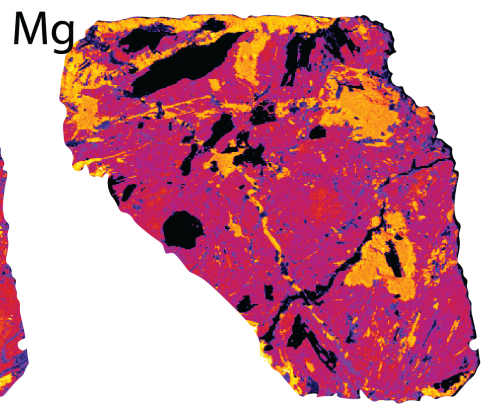
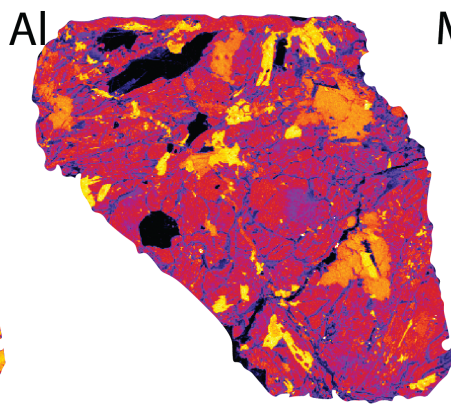
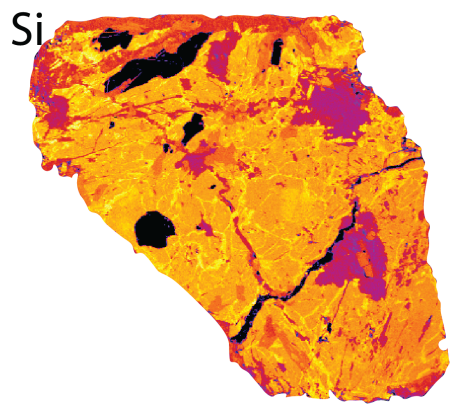
760 **Figure 9:** Pressure–temperature estimates from real subducted rocks and numerical models.
761 Grey arrow indicates the P – T path of this study. a) Real rock dataset of Penniston-Dorland et
762 al. (2015). b) Real rock dataset of Brown and Johnson (2018), including all low temperature-
763 high pressure datasets. c) Real rock dataset of Agard et al. (2018), data from mélanges is
764 indicated as circles. d) Prograde pressure-temperature paths taken from the top of subducting
765 slabs from numerical models of Gerya et al. (2002), Syracuse et al. (2010), van Keken et al.
766 (2011) and Ruh et al (2015).

767

768 **Figure 10:** Schematic model for formation and exhumation of the blueschist chip. Structure of
769 subduction zone after Fryer et al. (1999), Oakley et al. (2008) and Pabst et al. (2012).
770 Schematic serpentinitisation after Ruh et al (2015). Blueschist clast indicated as purple star. The
771 mechanism of exhumation of the blueschist clast from ca. 50 km ca. 49 Ma ago to the shallow
772 region under the forearc before the last 3 Ma is unknown.
773

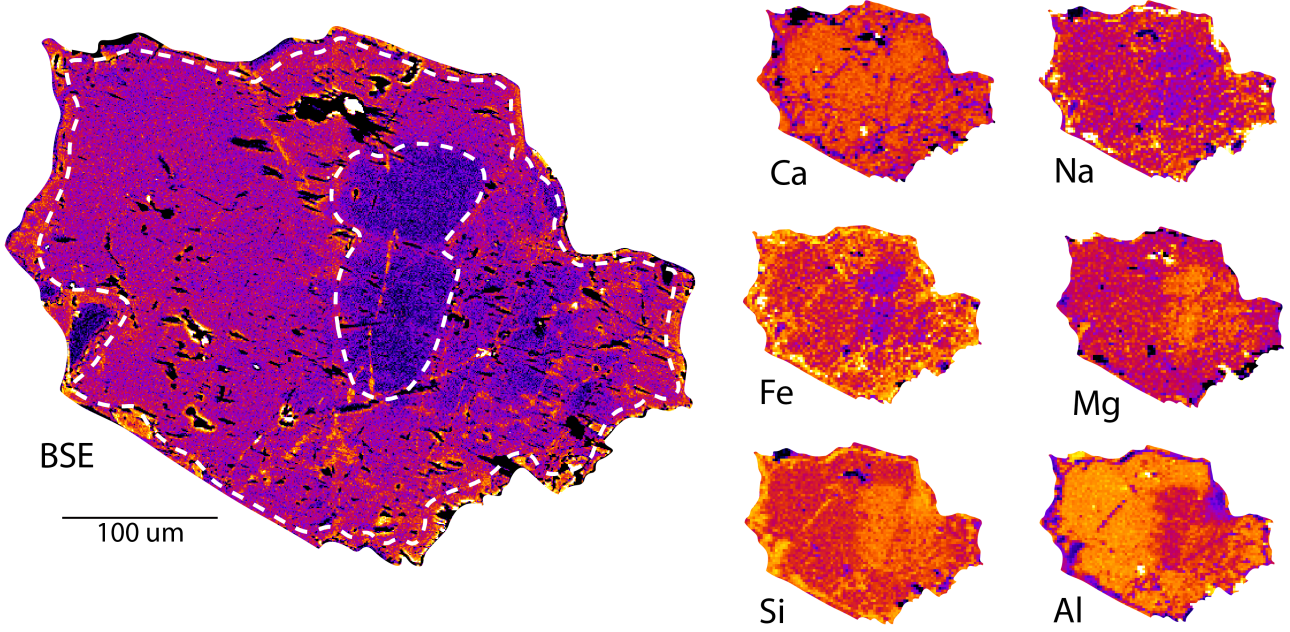






1 mm

a) Amphibole



b) Chlorite

